


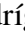



Rings and arcs around evolved stars – III. Physical conditions of the ring-like structures in the planetary nebula IC 4406 revealed by MUSE

G. Ramos-Larios^{★1} , J. A. Toalá² , J. B. Rodríguez-González² , M. A. Guerrero³ 
and V. M. A. Gómez-González^{2,4} 

¹Instituto de Astronomía y Meteorología, Dpto. de Física, CUCEI, Univ. de Guadalajara, Av. Vallarta 2602, Arcos Vallarta, 44130 Guadalajara, Mexico

²Instituto de Radioastronomía y Astrofísica (IRyA), UNAM Campus Morelia, Apartado postal 3-72, 58090 Morelia, Michoacán, Mexico

³Instituto de Astrofísica de Andalucía, IAA-CSIC, Glorieta de la Astronomía S/N, E-18008 Granada, Spain

⁴Institute for Physics and Astronomy, Universität Potsdam, Karl-Liebknecht-Str. 24/25, D-14476 Potsdam, Germany

3 March 2022

ABSTRACT

We present the analysis of Very Large Telescope (VLT) Multi Unit Spectroscopic Explorer (MUSE) observations of the planetary nebula (PN) IC 4406. MUSE images in key emission lines are used to unveil the presence of at least 5 ring-like structures North and South of the main nebula of IC 4406. MUSE spectra are extracted from the rings to unambiguously assess for the first time in a PN their physical conditions, electron density (n_e) and temperature (T_e). The rings are found to have similar T_e than the rim of the main nebula, but smaller n_e . Ratios between different ionic species suggest that the rings of IC 4406 have a lower ionization state than the main cavity, in contrast to what was suggested for the rings in NGC 6543, the Cat’s Eye Nebula.

Key words: stars: evolution — stars: winds, outflows — (ISM:) planetary nebulae — (ISM:) planetary nebulae: individual (IC 4406)

1 INTRODUCTION

Ring-like structures have been detected around evolved low- and intermediate-mass stars ($1 M_{\odot} \lesssim M_i < 8 M_{\odot}$) in optical, IR and radio observations (see, e.g., [Mauron & Huggins 2006](#); [Balick et al. 2012](#); [Corradi et al. 2004](#); [Phillips et al. 2009](#); [Ramos-Larios et al. 2011](#); [Cernicharo et al. 2015](#)). Such structures have been classified as (complete) rings, arcs, elliptical structures and spirals. They can be found in different stages of the evolution of those stars including asymptotic giant branch (AGB) stars, planetary nebulae (PNe), and sources in the intermediate proto-PN (pPN) evolutionary phase ([Ramos-Larios et al. 2016](#), hereinafter Paper I). Throughout the present letter, we will refer to these structures simply as rings.

Different formation scenarios have been proposed in the literature, including the intrinsic variability of the wind of the AGB progenitor (e.g. [Zijlstra et al. 2002](#)), solar-like inversions of the stellar magnetic field (e.g. [García-Segura et al. 2001](#)), or the viscous coupling between the outflowing gas and dust components (e.g. [Simis et al. 2001](#)) to mention a few (see, e.g., [Guerrero et al. 2020](#), for a review; hereafter Paper II). The formation scenario supported by the largest number of observational and numerical results rather involves the modulation of the AGB wind by the presence of a companion (e.g. [Mastromaros & Morris 1999](#); [Maercker et al. 2012](#)). Moreover, modern numerical simulations have shown that the variety of rings can be explain by the 3D spirals patterns produced by a binary depending on the viewing angle (see [He 2007](#); [Kim et al. 2019](#); [El Mellah et al. 2020](#), and references therein). Recent ALMA observations of AGB stars further

suggest that sub-stellar companions might be able to produce similar structures ([Decin et al. 2020](#)).

In Paper I we presented a search and characterization of rings around evolved low-and intermediate-mass stars using archival *Hubble Space Telescope* (*HST*) and *Spitzer Space Telescope* observations. Accounting for rings reported in the literature, we found that only 8% of a sample of ~ 650 objects exhibited any form of these structures. The reasons for such small occurrence may be twofold (possibly not excluding each other): the ring structures are less bright than the central cores of PNe and these structures are not present around all those evolved stars.

Detailed studies of rings around AGB stars have been relatively easy to achieve using sub-millimeter observations, proving to be one of the most powerful tools to study the velocity, density and temperature of spiral structures using their molecular emission. Subsequent modeling of the spirals give us information on the orbital parameters of the binary system (see, e.g., [Cernicharo et al. 2015](#); [Kerschbaum et al. 2017](#); [Doan et al. 2020](#)).

On the other hand, rings around pPNe and PNe seem to be more difficult to characterize. The expansion of the ionized rim that gives birth to the PN distorts the shape and even destroys the surrounding ring-like features (see Paper II). Moreover, the main nebular shells are much brighter than the rings, requiring special processing to be applied to the images (see Paper I, and references therein). Studies of multi-epoch high-quality optical images obtained with the *HST* as those presented by [Balick et al. \(2001, 2012\)](#) and Paper II have successfully studied the expansion rates of the ring structures in the AGB C-rich star AFGL 3068, the pPNe CRL 2688, and the PNe NGC 6543, NGC 7009 and NGC 7027. Nevertheless, the information on the physical properties of the ring-like structures, their electron

★ E-mail: gerardo@astro.iam.udg.mx

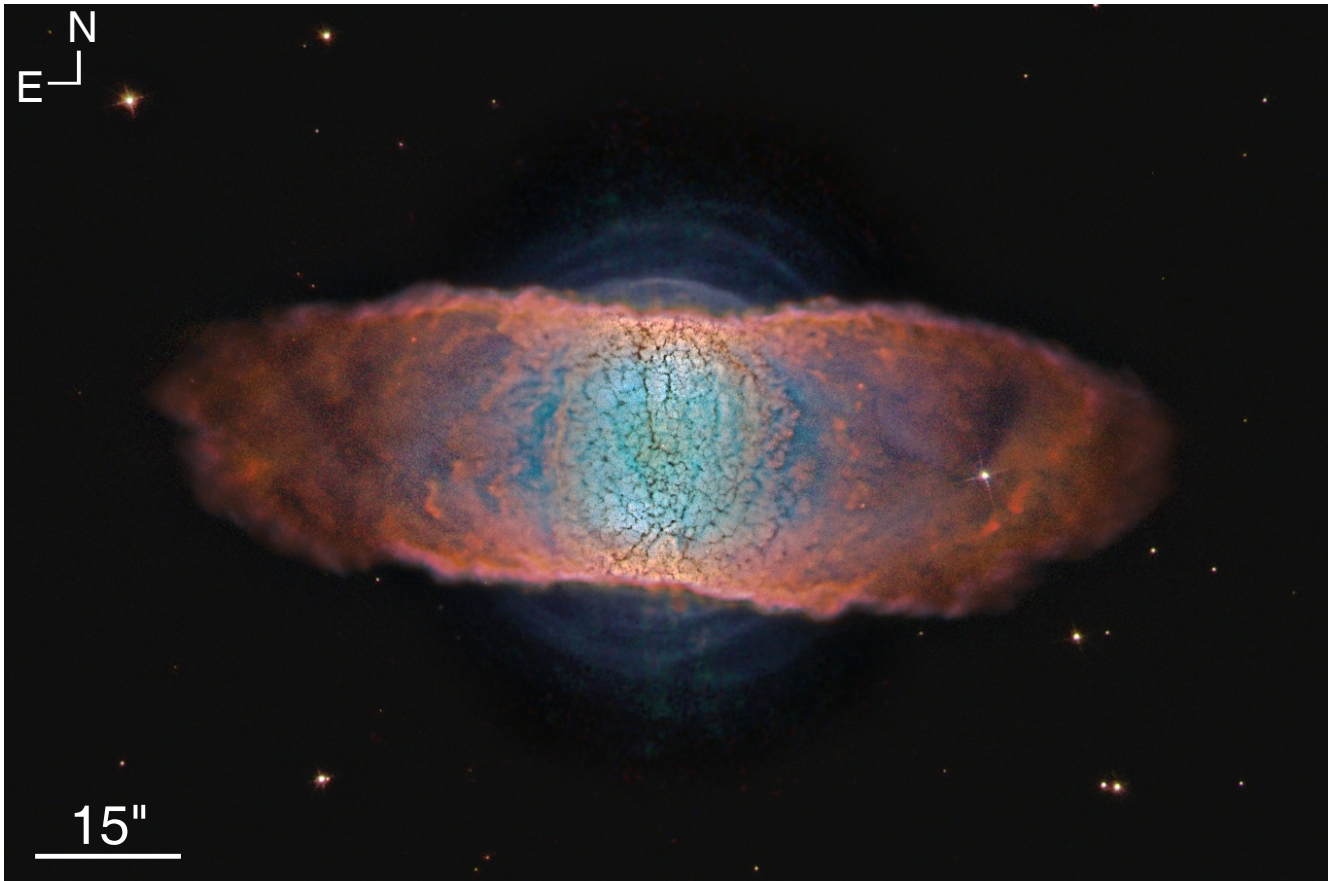


Figure 1. Hybrid VLT MUSE+*HST* WFPC2 color composite optical image of IC 4406 ([O III] – blue, H α – green and [N II] – red for *HST* and [O III] – blue, [O I] – cyan, H α – green, [N II] – orange and [S II] – red for MUSE). A series of ring-like structures North and South of the main nebula are clearly revealed thanks to the detailed MUSE-AOF data.

temperature (T_e) and density (n_e), has not been properly investigated yet.

We present here the physical properties found in the ring system around a PN, namely IC 4406, using the Integral Field Spectroscopic (IFS) technique that has been used to produce detailed studies of the two-dimensional variation of the excitation, ionization and chemical abundances of PNe (Walsh et al. 2018; Walsh & Monreal-Ibero 2020; Monreal-Ibero & Walsh 2020, e.g.) and to unveil their spatio-kinematic structure (e.g., Guerrero et al. 2021a).

IC 4406 is a barrel-like bipolar PN with a bright waist and filamentary structures in the bipolar lobes (see Figure 1). The waist can be interpreted as a toroidal structure surrounded by a dense torus of dust, whereas the bipolar lobes can be linked to CO ($J = 2 \rightarrow 1$) high-velocity flows along the nebular major axis (Cox et al. 1991; Sahai et al. 1991). In Paper I we reported the presence of 3 rings in IC 4406 immediately outside the dusty torus, two North of the bright waist and one fainter to its South.

Here we use archival Very Large Telescope (VLT) Multi Unit Spectroscopic Explorer (MUSE) observations of IC 4406 (see Fig. 1), which provide unprecedented images and spectra of the rings around this PN to investigate their spatial distribution and physical conditions.

The observations used in this work are presented in Section 2, the images extracted from the IFS observations are described in Section 3, and the physical conditions of the rings are computed in Section 4. Discussion and conclusions are presented in Section 5.

2 OBSERVATIONS

IC 4406 was observed by the VLT MUSE on 2017 June 16 with a total exposure time of 180 s (Program ID 60.A-9100; Obs. ID. 1755413). The observations cover the 4700–9350 Å wavelength range with a spectral resolution of $R=3014$ and a pixel scale of $0.2 \text{ arcsec pix}^{-1}$.

The Adaptive Optics Facility (AOF) instrument was used during the observations to compensate for atmospheric effects aiming at obtaining a sharper view. The AOF includes the Four Laser Guide Star Facility (4LGSF), whose beams make sodium (Na) atoms glow in the upper atmosphere imitating stars, and the Ground Atmospheric Layer Adaptive Corrector for Spectroscopic Imaging (GALACSI), which corrects the turbulence by means of a deformable secondary mirror. It is worth noting that the AOF uses a dichroic filter to block the light in the 5800 to 6000 Å wavelength range, blocking the Na laser light from the detector.

The processed data were retrieved from the ESO Archive Science Portal¹.

Images and spectra were extracted from the MUSE cube using the QFitsView analysis software². Preliminary spectra obtained by averaging over the brightest northern ring-like structures were obtained to identify the most prominent emission lines in order to produce images emphasizing the rings.

¹ <http://archive.eso.org/scienceportal/home>

² <https://www.mpe.mpg.de/~ott/QFitsView/>

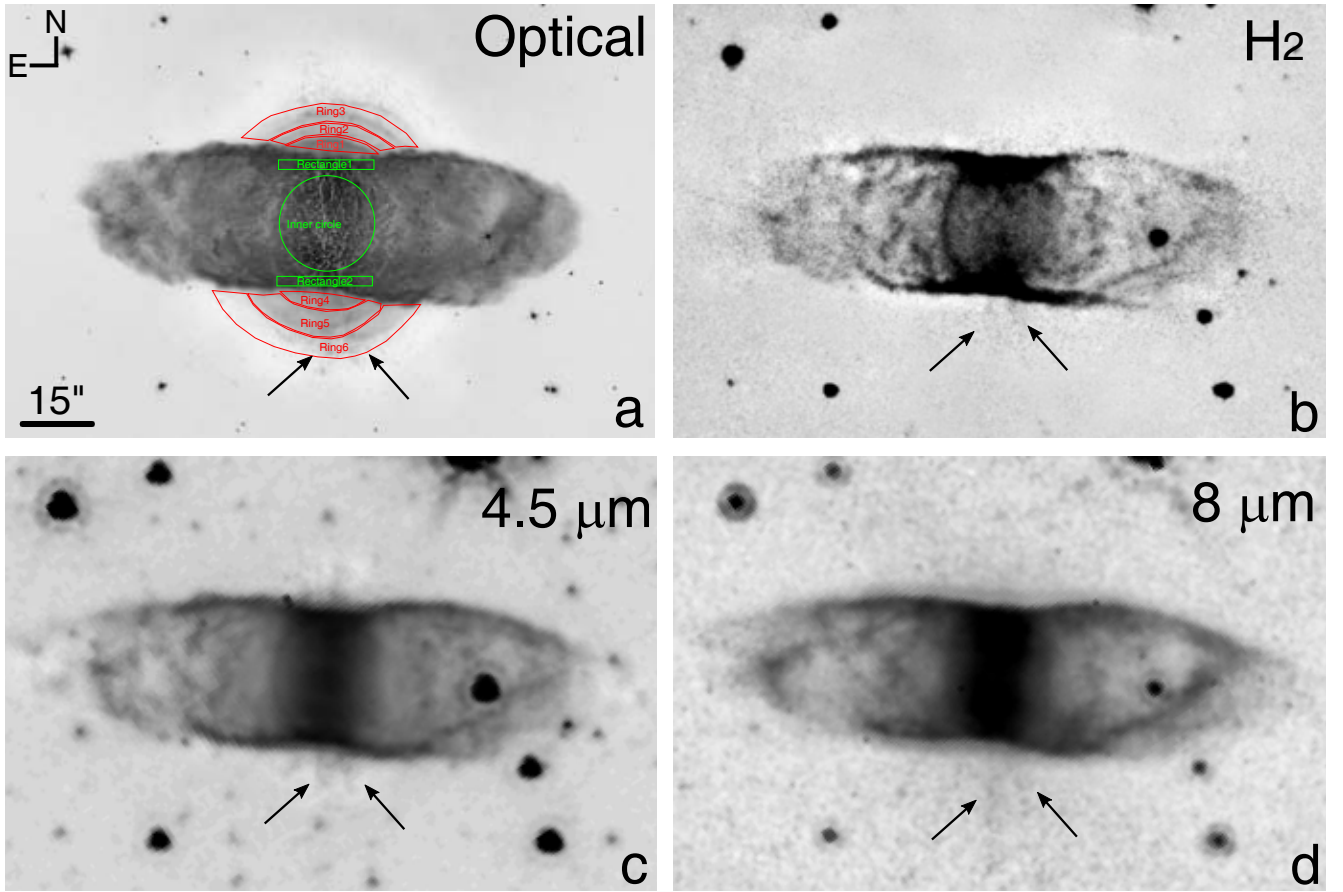


Figure 2. (a) Grey-scale representation of the hybrid image presented in Figure 1. Spectra of the arc-like features are extracted from the red annulus sector apertures numerated from 1 to 6, and spectra of the main nebula from the green circular and rectangular regions (see text for details). (b) CFHT near-IR H_2 1–0 S(1) narrow-band image of IC 4406. (c) and (d) *Spitzer* IRAC images of IC 4406 in the $4.5 \mu\text{m}$ and $8 \mu\text{m}$ bands, respectively. The black arrows in all the images point to faint radial streaks described in Section 3.

To create high-quality images, we retrieved *HST* WFPC2 images from the Hubble Legacy Archive³ obtained on 2001 June 28 and 2002 January 19 (Prop. ID 8726 and 9314). Images obtained in the F502N ($\lambda_c = 5012 \text{ \AA}$, FWHM = 26.9 \AA), F656N ($\lambda_c = 6564 \text{ \AA}$, FWHM = 21.5 \AA), and F658N ($\lambda_c = 6591 \text{ \AA}$, FWHM = 28.5 \AA) narrow-band filters were downloaded to produce images in the $[\text{O III}] \lambda 5007 \text{ \AA}$, $H\alpha$, and $[\text{N II}] \lambda 6584 \text{ \AA}$ emission lines, respectively.

The observations for both epochs consisted of series of three exposures with exposure times of 600 s for the $[\text{O III}]$ filter and 540 s for the $H\alpha$ and $[\text{N II}]$ filters. We also use in our composition the image downloaded from the website [https://commons.wikimedia.org/wiki/File:IC_4406_\"Retina\".png](https://commons.wikimedia.org/wiki/File:IC_4406_\).

Figure 1 presents a color-composite, hybrid MUSE+*HST* nebular image of IC 4406. The hybrid composition is actually the result of layering two separate frames of the same object obtained using different instruments (in this case, the *HST* WFPC2 and VLT MUSE). This technique, extensively used by our group (see, e.g., Guerrero et al. 2021a,b; Sabin et al. 2021; Toalá et al. 2021; Ramos-Larios et al. 2018, and references therein), registers the lower-resolution VLT MUSE image to match the higher-resolution *HST* WFPC2 image. In particular, the *HST* images were combined with narrow-band images extracted from the MUSE data cube in the emission lines of $[\text{O III}]$

$\lambda 5007 \text{ \AA}$, $[\text{O I}] \lambda 6300 \text{ \AA}$, $H\alpha$, $[\text{N II}] \lambda 6584 \text{ \AA}$, and $[\text{S II}] \lambda 6731 \text{ \AA}$. This procedure enhances the small-scale structures and fine details features of the main nebula present in the *HST* image and emphasizes the outer emission mainly from the rings and high- and low-ionization structures present in the MUSE data.

A gray scale version of this image is presented in Figure 2-a.

For comparison and discussion we also obtained archival near-IR H_2 images from the 3.6 m Canada-France-Hawaii Telescope (CFHT) IR camera (CFHTIR), which uses a 1024×1024 Rockwell HAWAII #142 detector with a pixel scale of $0.2 \text{ arcsec pix}^{-1}$. A series of ten exposures 180 s long were acquired on 2004 May 4 (Program ID 04AT02, P.I. Sun Kwok) through the H_2 1–0 S(1) ($\lambda_c = 2.122 \mu\text{m}$) filter. The images were combined and stacked for the final composition shown in Figure 2-b.

Finally, we also retrieved *Spitzer* IRAC data from the Spitzer Heritage Archive⁴. The observations were performed on 2004 March 5 under the Program ID 68 (PI: G. Fazio). *Spitzer* IR images of IC 4406 are also shown in Figure 2-c and d.

³ <https://hla.stsci.edu/>

⁴ <https://sha.ipac.caltech.edu/applications/Spitzer/SHA/>

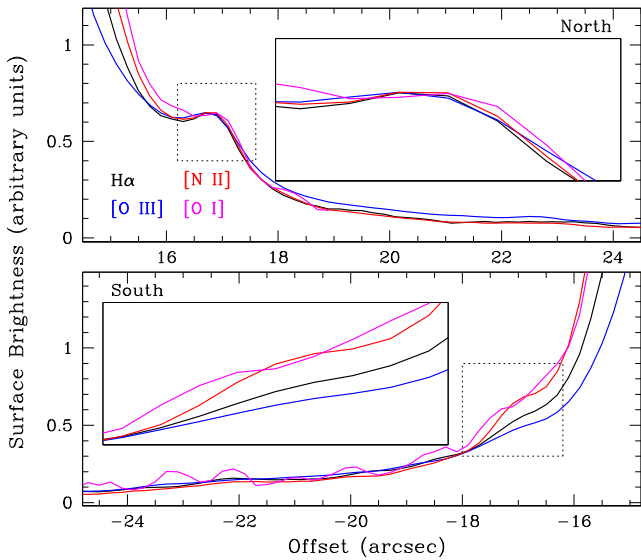


Figure 3. Surface brightness spatial profiles of the rings of IC 4406 along PA 358° at the North (top) and PA 178° at the South (bottom) of its main nebular shell in the $H\alpha$ (black), $[O\ III]\ \lambda 5007\ \text{\AA}$ (blue), $[N\ II]\ \lambda 6584\ \text{\AA}$ (red), and $[O\ I]\ \lambda 6300\ \text{\AA}$ (magenta) emission lines. The dotted inset is zoomed into the solid box to emphasize the spatial offsets between different emission lines that reveal the rings ionization structure.

3 IMAGERY

The main (bright) body of IC 4406, the elongated barrel-like structure, is detected in a wealth of emission lines. This is not the case for the rings, however, which are best detected in the $[O\ III]\ \lambda 5007\ \text{\AA}$ emission line image. The hybrid image presented in Figure 1 suggests the presence of a series of at least 5 arcs northern and southern of IC 4406 extending to distances up to 30 arcsec from the central star, with the innermost northern arc being the brightest one. These images demonstrate that the ring-like structures do not have a coherent shape, i.e. they do not seem to correspond to sections of complete circular structures, neither spirals. They are rather consistent with interlaced arcs projected onto the plane of the sky disrupted along the E-W direction by the expansion of the PN.

The optical and IR images of IC 4406 presented in Figure 1 and 2 reveal the presence of radial streaks protruding from the inner cavity of IC 4406 and pointing toward the position of the central star (black arrows in these figures). These rays can also be hinted in the *Spitzer* $4.5\ \mu\text{m}$ image, as well as in the H_2 image, although weaker and less extended (see other panels in Fig. 2). These structures can be caused by clumps in the main nebular shell that would produce an azimuthally non-uniform photoionization of the outermost nebular regions. Indeed, the optical grey-scale image presented in Figure 2-a shows that these radial streaks are detected farther than the rings. This implies the azimuthally variable ionization of the arcs, which, according to Paper II, induces azimuthally non-uniform variations in the pressure of the gas that can be expected to affect the shape of the arcs, leading ultimately to their disruption.

To peer into the ionized structure of the rings, surface brightness profiles of emission lines that map the rings have been extracted along directions of interest. Figure 3 shows the $H\alpha$, $[N\ II]\ \lambda 6584\ \text{\AA}$, $[O\ I]\ \lambda 6300\ \text{\AA}$, and $[O\ III]\ \lambda 5007\ \text{\AA}$ profiles extracted from the northern (PA= 358°) and southern (PA= 178°) rings. Whereas the $H\alpha$, $[N\ II]$, and $[O\ III]$ lines exhibit almost identical profiles, peaking at the same positions, this is not the case for the $[O\ I]$ emission.

The peak of the latter is displaced outwards, with the $[O\ I]$ emission peaks of the brightest northern and southern ring shifted by $\approx 0''.2$ and $\approx 0''.3$, respectively, with respect to those of the other emission lines. This unveils a notable ionization stratification of the rings, most likely associated with a photoionization front, as shocks in a low-density medium are expected to produce inverted ionization structures instead (e.g., IC 4634, Guerrero et al. 2008).

4 PHYSICAL CONDITIONS OF THE RINGS

We extracted several spectra from a number of apertures probing different regions within IC 4406. Six of these spectra correspond to the rings at the northern and southern regions from IC 4406 (red annulus sectors in Fig. 2-a). These spectra are presented in Figure 4.

Spectra from the outermost rings were also extracted, but their low signal-to-noise ratio (S/N) hampered any further spectral analysis. The extracted spectra were corrected for extinction by using the $c(H\beta)$ value estimated for each region from the Balmer decrement method corresponding to a case B photoionized nebula of $T_e = 10,000\ \text{K}$ and $n_e = 1000\ \text{cm}^{-3}$ (Osterbrock & Ferland 2006) and the reddening curve of Cardelli et al. (1989) with $R_V=3.1$.

For control and comparison, we also extracted three additional spectra, one from a circular aperture at the center of IC 4406 representative of high-excitation regions and two rectangular apertures on the northern and southern rim of IC 4406 representative of low-excitation regions. The extraction regions in green corresponds to a circular aperture with radius 9.5 arcsec as shown in Figure 2-a, which will now be referred as Inner Circle, and two rectangular regions of 19×1.8 arcsec in size referred as Rectangle 1 and 2, respectively. The spectral analysis has been performed using IRAF (Tody 1993) standard routines.

Table 1 presents the complete list of lines detected from the spectra of IC 4406 extracted from different regions. Dereddened intensities relative to an arbitrary value 100 for $H\beta$ are also listed in this table. Table 1 corroborates previous statements indicating that the $[O\ III]\ 5007\ \text{\AA}$ emission line dominates in the rings (see Paper II, and references therein), followed by the $[N\ II]\ 6583\ \text{\AA}$ emission line. The available emission lines allowed us to compute T_e using the $[N\ II]$ and $[S\ III]$ auroral-to-nebular line ratio⁵ and n_e using the $[S\ II]\ \lambda\lambda 6717, 6730\ \text{\AA}$ and $[Cl\ III]\ \lambda\lambda 5518, 5538\ \text{\AA}$ doublet line ratios. This calculation has been performed using the IRAF task *temden*. The estimated values of T_e and n_e are listed in the bottom section of Table 1.

The spectra extracted from the inner rings (Ring 1 and 4) resulted in $n_e \approx 700\ \text{cm}^{-3}$ and $T_e \approx 12,000\ \text{K}$. The spectra of the most external rings (not shown here) did not detect the necessary emission lines to calculate n_e and T_e . On the other hand, the spectra obtained for the Rectangle 1 and 2 extractions exhibit a large number of emission lines with higher S/N (see last two columns of Table 1). For these spectra, the diagnostic-sensitive line ratios implied n_e in the range 900 to $1,000\ \text{cm}^{-3}$ and T_e in the range 11,500 to 13,100 K.

5 DISCUSSION AND CONCLUSIONS

The detection of ring-like structures in PNe has been a difficult task in the past (see Paper I). The determination of their physical conditions has been even more challenging as the high-quality spectroscopic

⁵ The value of $T_e([O\ III])$ could not be computed as the spectral range of the MUSE data does not include the $[O\ III]\ 4363\ \text{\AA}$ auroral emission line.

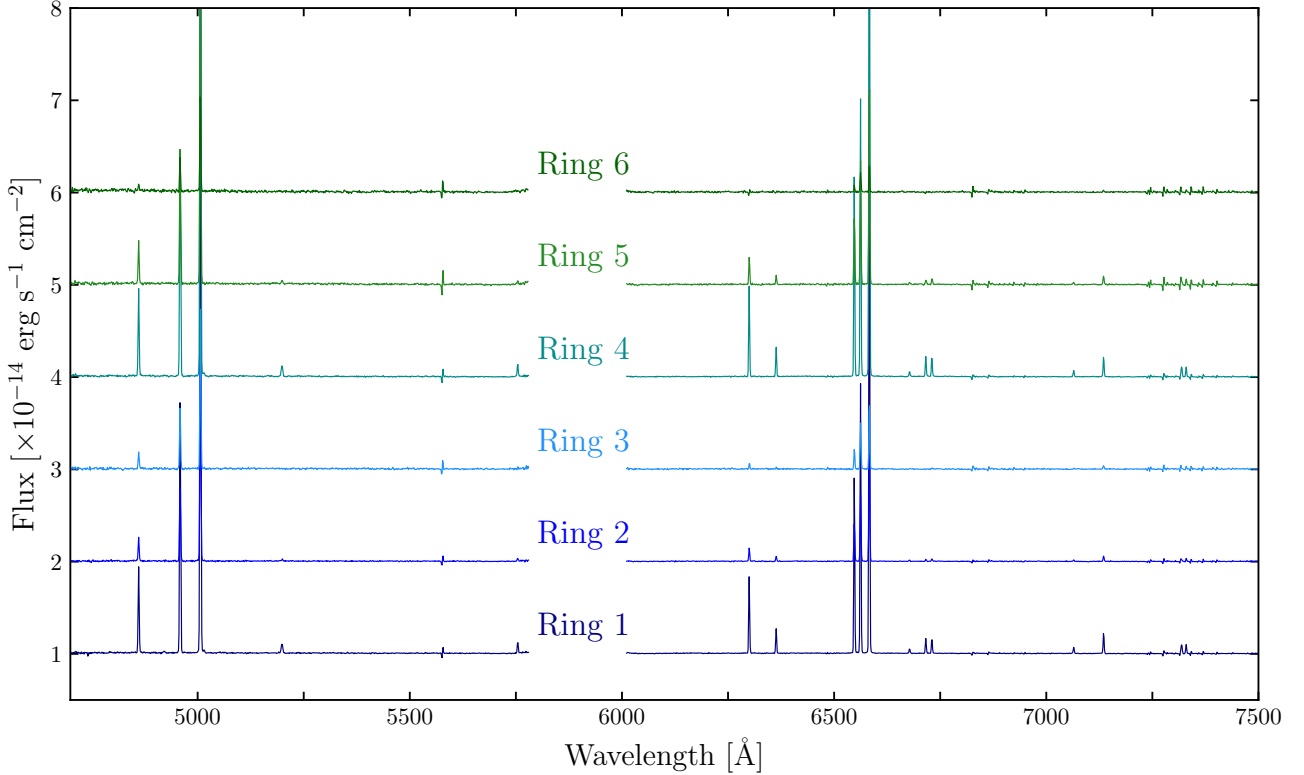


Figure 4. VLT MUSE spectra in the 4700–7500 Å wavelength range of ring-like features in IC 4406 extracted from the six red apertures overlaid in Figure 2-a. Note that the AOF dichroic filter blocks the light in the 5800 to 6000 Å wavelength range.

data required to detect the temperature and density sensitive emission lines of the elusive ring emission were lacking. IFS observations offer the means to obtain direct determinations of the physical conditions n_e and T_e of the ring-like structures in any PN using spectra. The analysis of the spectra extracted from the MUSE data indicates that n_e decreases from 900–1,000 cm^{-3} in the main cavity and rim of IC 4406 to $\sim 700 \text{ cm}^{-3}$ for the first outer rings where the density determination is more reliable. Meanwhile T_e is virtually the same for the rim of IC 4406 and the first outer rings (see Table 1), with some evidence of larger temperatures for the innermost regions.

We can use the emission line intensities, n_e , and T_e values listed in Table 1 to assess possible ionization differences between the main nebular shell of IC 4406 and its ring-like structures.

Using the expressions listed in table 3 of Alexander & Balick (1997), we calculated the ionic ratios listed in Table 2 and presented in Figure 5 for a better inspection. Compared to the inner regions of the main nebula, the nebula edge and the ring-like features are characterized by a lower ionization stage, with lower values of the O^{++}/O^0 and O^{++}/O^+ ratios (Fig. 5). Meanwhile the O^+/O^0 ratio is notably flat across the different nebular structures. The N^+/O^+ ionic ratios in the ring-like features are also similar to those of the nebular rim, whereas it is consistent for the innermost nebula given the large uncertainty for this value. If this ratio is assumed to represent the N/O abundance ratio, as usually adopted (Kingsburgh & Barlow 1994), this would indicate similar N/O abundance ratio for the outer rings and main nebula.

Similar calculations have only been attempted for NGC 6543, the Cat’s Eye Nebula (Balick et al. 2001). These authors used narrow-

band *HST* images and spectra of the inner core of NGC 6543 to suggest that the rings shared similar properties as that of the main nebula, which is in contrast with the results of the analysis of the MUSE data of IC 4406 here presented. Further analysis of high-quality spectra of ring-like structures are most needed to assess their physical structure and ionization stage.

Finally, we note the spatial shift of the peak intensity of the [O I] emission with respect to the other emission lines. This reveals a notable ionization stratification within the rings.

ACKNOWLEDGMENTS

GR-L acknowledges support from CONACyT grant 263373 and PRODEP (Mexico). VMAGG acknowledges support from the Programa de Becas posdoctorales of the Dirección General de Asuntos del Personal Académico (DGAPA) of the Universidad Nacional Autónoma de México (UNAM, Mexico). VMAGG and JAT acknowledge funding by DGAPA UNAM PAPIIT project IA100720. JAT also acknowledges support from the Marcos Moshinsky Foundation (Mexico). JBR-G thanks CONACyT for a student scholarship. MAG acknowledges support of the Spanish Ministerio de Ciencia, Innovación y Universidades grant PGC2018-102184-B-I00, co-funded by FEDER funds. Based on observations made with the NASA/ESA Hubble Space Telescope, and obtained from the Hubble Legacy Archive, which is a collaboration between the Space Telescope Science Institute (STScI/NASA), the Space Telescope European Coordinating Facility (ST-ECF/ESA) and the Canadian Astronomy Data

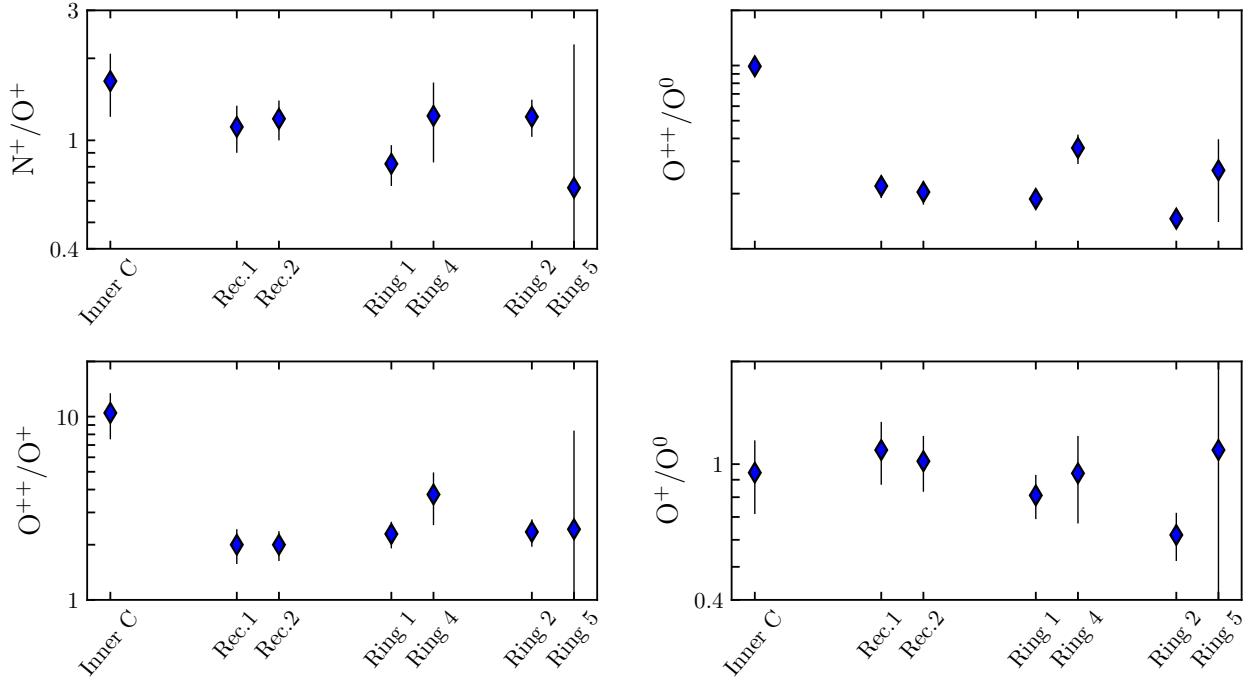


Figure 5. Ionic ratios obtained for different regions in IC 4406. These results are also listed in Table 2. The dots are distributed according to the distance of each region to the central star.

REFERENCES

- Alexander, J. & Balick, B. 1997, *AJ*, 114, 713. doi:10.1086/118505
- Balick, B., Gomez, T., Vinković, D., et al. 2012, *ApJ*, 745, 188. doi:10.1088/0004-637X/745/2/188
- Balick, B., Wilson, J., & Hajian, A. R. 2001, *AJ*, 121, 354. doi:10.1086/318052
- Cardelli, J. A., Clayton, G. C., & Mathis, J. S. 1989, *ApJ*, 345, 245. doi:10.1086/167900
- Cernicharo, J., Marcelino, N., Agúndez, M., et al. 2015, *A&A*, 575, A91. doi:10.1051/0004-6361/201424565
- Corradi, R. L. M., Sánchez-Blázquez, P., Mellema, G., et al. 2004, *A&A*, 417, 637. doi:10.1051/0004-6361:20034420
- Cox, P., Huggins, P. J., Bachiller, R., et al. 1991, *A&A*, 250, 533
- Decin, L., Montargès, M., Richards, A. M. S., et al. 2020, *Science*, 369, 1497. doi:10.1126/science.abb1229
- Doan, L., Ramstedt, S., Vlemmings, W. H. T., et al. 2020, *A&A*, 633, A13. doi:10.1051/0004-6361/201935245
- Guerrero, M. A., Ramos-Larios, G., Toalá, J. A., et al. 2020, *MNRAS*, 495, 2234. doi:10.1093/mnras/staa1225
- Guerrero, M. A., Cazzoli, S., Rechy-García, J. S., et al. 2021, *ApJ*, 909, 44. doi:10.3847/1538-4357/abe2aa
- Guerrero, M. A., Ortiz, R., Sabin, L., et al. 2021, *MNRAS*, 501, 3594. doi:10.1093/mnras/staa3082
- He, J. H. 2007, *A&A*, 467, 1081. doi:10.1051/0004-6361:20066435
- Kerschbaum, F., Maercker, M., Brunner, M., et al. 2017, *A&A*, 605, A116. doi:10.1051/0004-6361/201730665
- Kim, H., Liu, S.-Y., & Taam, R. E. 2019, *ApJS*, 243, 35. doi:10.3847/1538-4365/ab297e
- Kingsburgh, R. L., Barlow, M. J., 1994, *MNRAS*, 271, 257. doi:10.1093/mnras/271.2.257
- Luridiana, V., Morisset, C., & Shaw, R. A. 2015, *A&A*, 573, A42. doi:10.1051/0004-6361/201323152
- Maercker, M., Mohamed, S., Vlemmings, W. H. T., et al. 2012, *Nature*, 490, 232. doi:10.1038/nature11511
- Marquez-Lugo, R. A., Ramos-Larios, G., Guerrero, M. A., et al. 2013, *MNRAS*, 429, 973. doi:10.1093/mnras/sts381
- Mastrodemos, N. & Morris, M. 1999, *ApJ*, 523, 357. doi:10.1086/307717
- Mauron, N. & Huggins, P. J. 2006, *A&A*, 452, 257. doi:10.1051/0004-6361:20054739
- Monreal-Ibero, A. & Walsh, J. R. 2020, *A&A*, 634, A47. doi:10.1051/0004-6361/201936845
- El Mellah, I., Bolte, J., Decin, L., et al. 2020, *A&A*, 637, A91. doi:10.1051/0004-6361/202037492
- Osterbrock, D. E. & Ferland, G. J. 2006, *Astrophysics of gaseous nebulae and active galactic nuclei*, 2nd. ed. by D.E. Osterbrock and G.J. Ferland. Sausalito, CA: University Science Books, 2006
- Phillips, J. P., Ramos-Larios, G., Schröder, K.-P., et al. 2009, *MNRAS*, 399, 1126. doi:10.1111/j.1365-2966.2009.15379.x
- Ramos-Larios, G., Phillips, J. P., & Cuesta, L. C. 2011, *MNRAS*, 411, 1245. doi:10.1111/j.1365-2966.2010.17756.x
- Ramos-Larios, G., Vázquez, R., Guerrero, M. A., et al. 2012, *MNRAS*, 423, 3753. doi:10.1111/j.1365-2966.2012.21165.x
- Ramos-Larios, G., Santamaría, E., Guerrero, M. A., et al. 2016, *MNRAS*, 462, 610. doi:10.1093/mnras/stw1572
- Ramos-Larios, G., Guerrero, M. A., Sabin, L., et al. 2017, *MNRAS*, 470, 3707. doi:10.1093/mnras/stx1519
- Ramos-Larios, G., Guerrero, M. A., Nigoche-Netro, A., et al. 2018, *MNRAS*, 475, 932. doi:10.1093/mnras/stx3256
- Sabin, L., Guerrero, M. A., Zavala, S., et al. 2021, *MNRAS*, 501, 3582. doi:10.1093/mnras/staa3270
- Sahai, R., Wootten, A., Schwarz, H. E., et al. 1991, *A&A*, 251, 560
- Toalá, J. A., Rubio, G., Santamaría, E., et al. 2021, *MNRAS*, 502, 4658. doi:10.1093/mnras/stab273
- Tody, D. 1993, *Astronomical Data Analysis Software and Systems II*, 52, 173
- Walsh, J. R. & Monreal-Ibero, A. 2020, *Galaxies*, 8, 31. doi:10.3390/galaxies8020031
- Walsh, J. R., Monreal-Ibero, A., Barlow, M. J., et al. 2018, *A&A*, 620, A169. doi:10.1051/0004-6361/201833445
- Wang, M.-Y., Muthumariappan, C., & Kwok, S. 2006, *Planetary Nebulae in*

